PAPER

Check for updates

Promoting sulfur adsorption using surface Cu sites in metal–organic frameworks for lithium sulfur batteries†

Avery E. Baumann,[a] Gabrielle E. Aversa,[a] Anindya Roy,[b] Michael L. Falk, [ID][bcd] Nicholas M. Bedford[e] and V. Sara Thoi [ID] *[a]

Despite the promise of high energy density in lithium sulfur (Li–S) batteries, this technology suffers from poor long-term stability due to the dissolution of polysulfides upon battery cycling. Metal–organic frameworks (MOFs) are shown to be effective cathode materials for Li–S batteries, but the nature of sulfur–host interactions in these porous materials is not well-understood. Herein, we provide a detailed analysis on material and chemical properties that have direct influence on sulfur adsorption and battery performance. Favorable binding sites in CuBTC, a MOF proven promising for sulfur adsorption, are identified and characterized by a combination of theoretical, thermogravimetric, spectroscopic, and electrochemical experiments. By manipulating MOF particle size, we further demonstrate that a high density of Cu-rich surface defects drastically improves both maximum discharge capacity and polysulfide retention. Battery cycling data illustrates the significance of these surface Cu sites for the uptake of dissolved polysulfides, which mitigates irreversible capacity loss. In the wider scope of materials development, our findings suggest the use of carefully engineered surface defects in inorganic nanomaterials may enhance sulfur capture in Li–S batteries. This study thus advances chemical understanding towards rational design of porous materials with great implications for energy storage, sulfur removal, chemical sensing, and environmental remediation.

Introduction

Sulfur has emerged as an important cathode material in the search for high energy density storage devices beyond lithium ion batteries. Lithium sulfur (Li–S) batteries utilize the redox chemistry of sulfur species to store and deliver multiple equivalents of electrons through the forming and breaking of covalent bonds.[1] The use of conversion chemistry, as opposed to intercalation chemistry, allows Li–S batteries to achieve high energy density of 2600 W h kg^{-1} compared to ~300 W h kg^{-1} in lithium ion batteries. A typical Li–S electrochemical device contains a sulfur/carbon (S/C) composite cathode and Li anode. During discharge, elemental sulfur is reduced to polysulfides and the Li ions from the anode are transported to the sulfur electrode. However, a major obstacle for this technology is the dissolution of these reduced polysulfide intermediates in the electrolyte solution. Termed the polysulfide shuttle, the dissolved sulfides can diffuse between the two electrodes during cycling and deposit an insulating layer of insoluble lithium sulfides on the Li anode that is detrimental to the lifetime and capacity of the battery.[2]

One strategy to ameliorate the polysulfide shuttle is to encapsulate sulfur in a porous matrix. A variety of porous materials for trapping polysulfides have been reported, including the use of ordered mesoporous carbons,[3–8] doped carbons,[9–11] and inorganic compounds.[12–15] For instance, Nazar and co-workers have shown that long range order in mesostructured carbons and the availability of Lewis basic sites can improve polysulfide retention in Li–S battery cycling.[4,8,9,16,17] In addition, copper and copper sulfides (CuS and Cu$_2$S) in carbon cathodes have been shown to mitigate polysulfide dissolution.[14,15] Recently, several groups have demonstrated the use of metal–organic frameworks (MOFs), a class of porous crystalline materials consisting of metal nodes connected by organic linkers in a 3D network, for sulfur encapsulation in Li–S batteries.[18–25] For instance, Wang, Li, and co-workers postulated that the small pore aperture of ZIF-8, a Zn-based MOF, led to a superior storage capacity over three other surveyed MOFs and demonstrated the importance of particle size for controlling the diffusion of polysulfides within the MOF.[21,25] The synthetic versatility coupled

[a]Department of Chemistry, Johns Hopkins University, Baltimore, Maryland 21218, USA. E-mail: sarathoi@jhu.edu

[b]Department of Materials Science and Engineering, Johns Hopkins University, Baltimore, Maryland 21218, USA

[c]Department of Mechanical Engineering, Johns Hopkins University, Baltimore, Maryland 21218, USA

[d]Department of Physics and Astronomy, Johns Hopkins University, Baltimore, Maryland 21218, USA

[e]Materials and Manufacturing Directorate, Air Force Research Laboratory, Wright-Patterson AFB, Ohio 45433, USA

† Electronic supplementary information (ESI) available: Additional thermogravimetric, spectroscopic and electrochemical data. See DOI: 10.1039/c8ta01057a

This journal is © The Royal Society of Chemistry 2018

J. Mater. Chem. A, 2018, **6**, 4811–4821 | 4811

with high stability and porosity make MOFs excellent platforms for probing the nature of sulfur adsorption and understanding polysulfide redox chemistry in porous materials.

One well-studied MOF, CuBTC (also known as HKUST-1) is composed of binuclear copper paddlewheel units and benzene-1,3,5-tricarboxylate (BTC) linkers. In the paddlewheel node structure, two copper atoms adopt a pseudo-octahedral geometry, where each is connected by four bridging carboxylates from BTC and is bound to an axial aqua ligand along the Cu–Cu vector.[26–28] This aqua ligand can be removed by thermal or chemical treatment, leaving the Cu sites coordinatively unsaturated and improving the metal's affinity for binding guest molecules (Scheme 1).[29] Previous studies show that sulfur species including dimethyl sulfide, hydrogen sulfide (H_2S), and *t*-butyl mercaptan are able to bind at this site.[30–33] The ability of the Cu framework to interact with sulfur makes it a strong candidate for Li–S battery systems, where these sites can chemically anchor sulfur and polysulfide guests.

Indeed, CuBTC has been previously examined as a cathode and separator material for Li–S energy storage devices.[20,21,24] However, in-depth chemical characterization of the sulfur-loaded CuBTC (CuBTC@S) has not been conducted, depriving a molecular understanding that would benefit rational design of new cathode materials. Herein, we identify favorable adsorption sites of sulfur in CuBTC and observe direct evidence of Cu–S binding. More importantly, we show that manipulation of particle size result in high polysulfide retention and improved battery performance. Our findings exemplify the complexity of polysulfide encapsulation and offer new strategies for using MOFs as a host for polysulfides in Li–S batteries.

Experimental

General

Benzene-1,3,5-tricarboxylic acid (BTC-H_3, 95%, Sigma-Aldrich), copper(II) nitrate ($Cu(NO_3)_2 \cdot 3H_2O$, 99.5%, Strem Chemicals), and elemental sulfur (S, 99.9%, Sigma Aldrich) were used
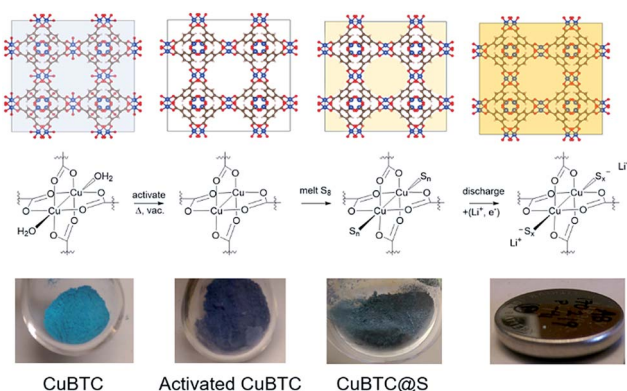
Scheme 1 Activation and sulfur loading of CuBTC. The top row qualitatively demonstrates the presence of water and sulfur in the pores of the solid state structure, while the middle row shows potential sites of binding at the Cu paddlewheel. The bottom row are photographs of the physical materials, illustrating the drastic color changes at each stage.

without further purification. Solvents including N,N-dimethylformamide (DMF, Sigma Aldrich), dichloromethane (DCM, Sigma Aldrich) and ethanol (EtOH, Decon Lab.) were also used as received. The structure and morphology of the CuBTC and CuBTC@S samples were characterized using powder X-ray diffraction (PXRD, Bruker D8 Focus diffractometer, Cu Kα, LynxEye detector), scanning electron microscopy (SEM, JEOL 6700F, 5 keV) equipped with an energy dispersive X-ray analyzer (EDS, EDAX Genesis 4000 X-ray Analysis System), and infrared spectroscopy (FT-IR, ThermoScientific Nicolet iS FT-IR with iD 5 ATR attachment). Thermogravimetric analysis (TGA) was conducted using a TA Instruments SDT Q600 under flowing Ar at a heating rate of 5.0 °C min^{-1}. UV-Vis spectra were obtained using a Cary 60 (Agilent Technologies). Raman measurements were performed using a Horiba Jobin-Yvon T64000 spectrometer equipped with an Olympus microscope, using the 514.5 nm line of the Spectra-Physics Ar$^+$ − Kr$^+$ laser for excitation. Atomic absorption spectra (AAS) were obtained using a Perkin Elmer AAnalyst 100 system and Perkin Elmer Intesitron hollow cathode lamps.

Material synthesis

Synthesis of 5.9 μm CuBTC. A previously reported solvothermal synthetic procedure was used.[20] In a 350 mL pressure vessel, 1.68 g (6.9 mmol) $Cu(NO_3)_2 \cdot 3H_2O$ and 0.92 g (4.4 mmol) BTC-H_3 were dissolved in a 200 mL solution of 1 : 1 (v/v) EtOH and DMF solution. The vessel was sealed using a threaded Teflon cap and shaken vigorously until all solids were dissolved. This sealed vessel was placed in a 120 °C oven and left undisturbed for 20 h. Once removed and cooled, light-blue solids were separated by centrifugation and washed 5 times with 40 mL EtOH. The washed solid was dried in air overnight to yield 1.7 g of a light-blue powder.

Synthesis of 0.16 and 1.6 μm CuBTC. A modified version of a previously reported "precooling" synthesis was used.[36] Two solutions of 1.0 g (4.8 mmol) BTC-H_3 in 40 mL EtOH and 3.4 g (14 mmol) $Cu(NO_3)_2 \cdot 3H_2O$ in 20 mL EtOH were separately cooled for 10 minutes before mixing the two solutions together while stirring. The final solution was allowed to warm to room temperature for 3 h. The light-blue solids were collected by centrifugation and washed a minimum of 7 times using 40 mL EtOH. The as-synthesized powders were dried in air overnight. A dry ice/acetone bath (−78 °C) and a dry ice/acetonitrile bath (−41 °C) were used for 0.16 μm CuBTC and 1.6 μm CuBTC, respectively.

Activation of CuBTC. The light-blue CuBTC powders were first chemically activated to remove water/solvent by repeated washing and soaking in 20 mL DCM over the course of 12 h (typically 8–10 times) until a royal blue color was observed.[29] The excess DCM was removed *in vacuo* and yielded a dark blue solid, which was then thermally activated by heating under vacuum at 180 °C for 15 min until a dark purple color was observed (Scheme 1).

Synthesis of CuBTC@S. Using the masses of unactivated MOF and sulfur, S : MOF loading ratios of 0.5, 1, or 1.5 were used. After activation, the CuBTC powders were transferred to

4812 | J. Mater. Chem. A, 2018, **6**, 4811–4821

This journal is © The Royal Society of Chemistry 2018

an Ar-filled glovebox, where the sulfur was added in a Schlenk flask along with a stainless steel ball. The flask was quickly sealed and evacuated to minimize exposure from the glovebox atmosphere. The sulfur and MOF powders were thoroughly mixed using a vortexer for 5 min and then heated to 155 °C for 10 h to allow the melted sulfur to diffuse into the MOF pores. Once cooled, the CuBTC@S powders appeared blue-green to dark green in color. Unless otherwise specified, 0.16, 1.6, and 5.9 μm CuBTC@S used in electrochemical measurements were synthesized using a S : MOF ratio of 1.5, which resulted in a typical S weight loading of ∼65% as determined by thermogravimetric analysis (Table S4†).

Cathode preparation. The cathode slurry was prepared using a 75 wt% CuBTC@S, 15 wt% Super-P carbon (99+%, Alfa Aesar), and 10 wt% poly(vinylidene fluoride) (PVDF, Alfa Aesar) solid mixture in *N*-methyl-2-pyrrolidinone (NMP, Oakwood Chemical). First, the CuBTC@S was mixed with PVDF binder thoroughly and then the Super-P carbon was added. This solid mixture was mixed using a vortexer for 5 minutes. The slurry was prepared by adding NMP to the mixture and homogenized on the vortexer for at least 30 min. The amount of NMP was measured by weight and is typically 4× the total mass of the solid mixture. After initial mixing, more NMP was added as needed to achieve a good slurry consistency that forms a homogeneous film after drying. Once homogenized, the slurry was cast onto pre-weighed 12.7 mm carbon paper discs and dried overnight in an 80 °C oven. The 12.7 mm cathodes were weighed again to determine the sulfur loading and stored in an Ar-filled glovebox.

CR 2032-type coin cells were constructed in an Ar-filled glovebox using a pre-weighed cathode, a polished metallic Li anode, two Celgard separators, two stainless steel spacers and spring, and 0.2 mL electrolyte. The electrolyte was composed of 1 M bis-(trifluoromethanesulfonyl)imide lithium (LiTFSI, Oakwood Chemical) in a mixed solution of 1,2-dimethoxyethane (DME, 99+%, Alfa Aesar) and 1,3-dioxolane (DOL, 99.5%, Acros Organics) (1 : 1, v/v) with an added 2 wt% lithium nitrate salt (LiNO$_3$, 99%, Strem Chemicals). Coin cells were used for electrochemical experiments with the cathode as the working electrode and the anode as both the counter and reference electrode.

Experimental methods

X-ray absorption spectroscopy

The local structure of Cu within MOF structures with and without S were examined using X-ray absorption spectroscopy (XAS). Experiments were performed at the 10-ID-B station of the Advanced Photon Source. Samples were prepared by uniformly spreading as-prepared powder across Kapton tape. Data was collected 200 eV below the Cu K-edge (8797 eV) up to ∼1000 eV past the edge. All data was processed in the program Athena, while EXAFS modeling was performed using the Artemis software package.[34] Scattering paths from Cu–O from the binding ligand, adjunct Cu atoms, and bound water molecules were modeled from the known crystal structure of CuBTC,[35] while Cu–S scattering paths were modeled from a modified CuBTC lattice where bound water molecules were replaced with S atoms.

Electrochemical measurements

Cyclic voltammetry (CV) was performed on an Ivium-n-STAT Multichannel Electrochemical Analyzer. Freshly prepared coin cells were used for CV where the potential was cycled at a scan rate of 0.1 mV s^{-1} between 2.9 and 1.6 V *vs.* Li/Li$^+$. Coin cells were cycled galvanostatically (MNT-BA-5V, MicroNanoTools) after resting for 8 h. All cells were charged and discharged cyclically at a C-rate of C/10 (168 mA g^{-1} S) for twenty cycles, followed by eighty cycles at C/5 (336 mA g^{-1} S). To obtain sufficient statistical significance, at least three of the same batteries were tested under the same conditions.

Polysulfide absorbance measurements

In an Ar-filled glovebox, an open cell was constructed using a polished Li metal anode as the counter electrode and the cathode material on an aluminum foil current collector as the working electrode. The prepared electrodes were carefully submerged in 5.0 mL of electrolyte solution in a 20 mL scintillation vial. As the cell was discharged under a constant current at a rate of C/20 (84 mA g^{-1} S), 0.3 mL aliquots were examined by UV-Vis absorbance spectroscopy. Foil is used instead of carbon paper for these cathodes due to the fragility of carbon paper during handling.

DFT calculations

The calculations presented in this work were performed with Vienna Ab initio Simulation Package (VASP).[37,38] Local density approximation (LDA)-based projector augmented wave (PAW) ultrasoft pseudopotentials were used.[37] The self-consistent calculations (SCF) and ionic relaxations with fixed lattice parameters had a plane-wave cutoff of 520 eV. The lattice parameters for CuBTC were obtained from previously reported crystallographic data.[35] A single *k*-point was used for the Brillouin zone integration due to the large unit cell of the MOF. Forces on ions were converged to less than 0.001 eV Å^{-1} for the entire unit cell and sulfur atoms.

The MOF unit cell was first ionically relaxed from the crystallographic unit cell and gave the value E(CuBTC). Configurations of neutral sulfur clusters obtained from previously published results[39] were relaxed, giving the value E(S), and inserted into different locations within the relaxed-MOF structure. First, the CuBTC structure was fixed and only the sulfur clusters were allowed to ionically relax until forces converged to less than 0.001 eV Å^{-1}. Once convergence was reached, the entire structure was again relaxed and resulted in the value E(CuBTC@S). The interaction distance is defined as the shortest distance between S and either Cu or C in the resulting relaxed structure. The interaction energy (ΔE_{int})[40] is then defined as:

$$\Delta E_{int} = E(CuBTC@S) - E(CuBTC) - E(S) \qquad (1)$$

This journal is © The Royal Society of Chemistry 2018

J. Mater. Chem. A, 2018, **6**, 4811–4821 | **4813**

Results and discussion

Characterization of sulfur adsorption sites in CuBTC

Density functional theory. As a first approach to probe these interactions, we used density functional theory (DFT) and detailed structural analyses to examine favorable sites for sulfur adsorption within CuBTC. Using previously reported structures of neutral S clusters in their lowest energy configuration,[39] S clusters of various lengths (S_n where $n = 1–8$) are simulated in the framework of the activated CuBTC at different positions and orientations (Fig. S1†). Upon relaxation, our calculations reveal the most favorable adsorption site is at the Cu paddlewheel unit. The Lewis acidic Cu centers are coordinatively unsaturated and are able to accept electron density from the S clusters to form strong Cu–S interactions.[20,41] DFT computation also shows a significant association between S clusters and the BTC π system. The electron withdrawing ability of carboxylic acids leads to a relatively electron-deficient aromatic system that can interact with the electron-rich S clusters.

The energy gained from introducing sulfur in these favorable sites is defined as the interaction energy (ΔE_{int}, eqn (1)).[40] The energy of the Cu–S interaction is more favorable than that of S–BTC in all cases except for S_1 atom (Fig. 1a). Although we do not expect the large sulfur chains to fragment extensively and form a single neutral S atom, the uncharacteristic ΔE_{int} obtained for the S_1–BTC case may be explained by the high symmetry of the singular atom. The symmetric bonding orbitals of S_1 may be more able to approach the aromatic π system and reorient itself to provide the most favorable orbital interaction. This hypothesis is supported by examining the S–BTC interaction distance, where S_1–BTC is more than 1 Å shorter than distances obtained for larger clusters (Fig. 1b). In addition, the S–MOF interaction distance increases as a function of S cluster size. This increase implies that the larger S clusters are unable to get close to the framework and adsorb as efficiently as the smaller clusters. As the calculated interaction energies are reflected in the S–MOF interaction distances, we introduce a cluster (S_5) in the center of the pore, nearly 5 Å away from BTC or Cu adsorption sites. The isolated cluster yields a negligible change in interaction energy and suggests that the metal nodes and organic linkers are critical for sulfur adsorption (Fig. 1a).
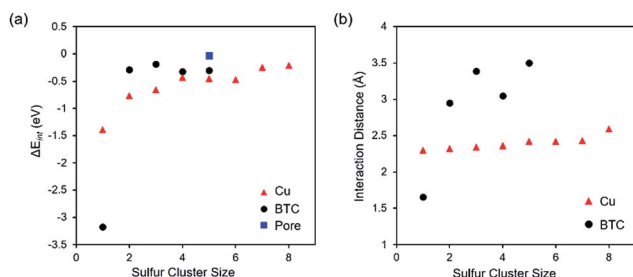
Although a crystallographic structure of CuBTC@S has previously been published,[42] the large disorder in S atoms in the MOF pores prevented the identification of S clusters and favorable adsorption sites. The chemical interactions discovered by DFT calculations thus provide a chemical model for understanding Cu–S interaction in CuBTC@S. We note that while our current approach focuses on neutral clusters, future computation on anionic polysulfide interactions in MOFs may lead to a greater understanding of how polysulfides anchor in porous materials during Li–S battery cycling.

X-ray absorption spectroscopy. Motivated by our computational results, we synthesize CuBTC with an average particle size of 5.9 μm using a reported solvothermal procedure.[20] We hypothesize that loading different concentrations of neutral sulfur would provide insights into the most favorable sulfur adsorption sites in the framework. Sulfur is loaded into CuBTC by using a previously reported melt infiltration technique.[20,43] A mixture of S_8 and activated CuBTC is ground and heated to 155 °C under vacuum for 10 h to allow for sulfur diffusion into the MOF. Interestingly, CuBTC@S samples with different S to MOF loading ratios of 0.5, 1.0, and 1.5 vary in color from blue to dark green with increased S-loading, signifying of differences in the coordination sphere of Cu.

To probe the effect of S loading on CuBTC, X-ray absorption spectroscopy (XAS) is performed to resolve local Cu structural changes with the MOF structure. XAS provides element-specific structural and chemical information and has been demonstrated to be a powerful tool for characterizing local structural changes around the metal centers in MOFs.[44–46] The X-ray absorption near-edge structure (XANES) spectra, shown in Fig. 2a, provides insights on Cu oxidation state and local structure of the CuBTC with varying amounts of S. As expected, XANES from all CuBTC samples exhibits a shift to higher edge energy (E_0) consistent with a Cu^{2+} oxidation, as evident by the similar in E_0 for CuO (Fig. 2a). Upon loading of S to a S : MOF ratio of 0.5, minor changes in XANES spectra are observable, with deviations becoming greater at higher energy. More strikingly, a pre-edge feature at 8987 eV is detected for this sample, which arises from 1s → 4p dipolar shakedown transition previously reported in CuBTC.[44] An increase in S : MOF ratio to 1.0 and 1.5 results in greater differences in the XANES from the pristine CuBTC, with a notable decrease in the white line intensity clearly evident. This decrease is an indication there is a comparative lack of electron occupancy in the 3d states, likely attributed to increased S–Cu interactions compared to the pristine and 0.5 S : MOF CuBTC samples.

The extended X-ray absorption fine structure (EXAFS) data is obtained by a conversion of the XAS data to k-space (k^2-weighted) (Fig. S2†), then Fourier transformed in r-space (Fig. 2b). The main features observed for unloaded CuBTC are consistent with previous results and can be attributed to backscattering from paddlewheel components including the BTC linker, the neighboring Cu atom, and the axial water ligand.[27,44,47] Differences in spectral features are observed with infiltration of S, along with the appearance of a new feature attributed to Cu–S interaction. This Cu–S feature increases in
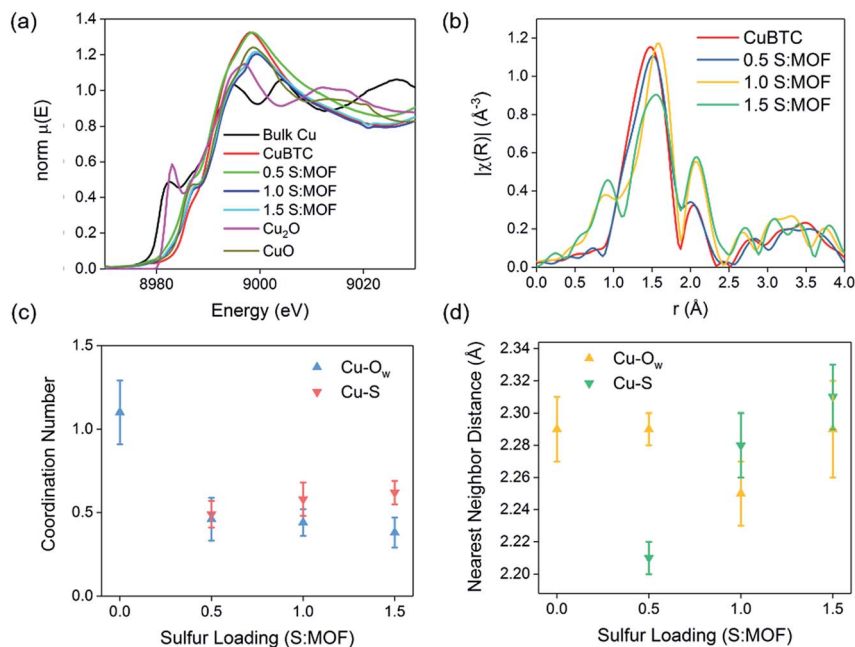

Fig. 1 (a) The interaction energy of sulfur adsorption in CuBTC as function of sulfur cluster size. In general, the Cu site (▲) is more favorable for sulfur interaction than at the BTC site (●) or the center of the pore (■). (b) The interaction distance of sulfur and nearest site on CuBTC as a function of sulfur cluster size. Larger clusters exhibit a greater interaction distance.

4814 | J. Mater. Chem. A, 2018, 6, 4811–4821

This journal is © The Royal Society of Chemistry 2018

Fig. 2 (a) XANES and (b) EXAFS profiles with (c) EXAFS modeling of Cu−S and Cu−O$_w$ (c) coordination number and (d) nearest neighbor distance as a function of S loading. The increase in Cu−S coordination number implies more Cu−S interaction as more sulfur fills the MOF. The increase in Cu−S nearest neighbor distances suggests a steric effect as larger S clusters are formed.

relative magnitude for the samples with a higher S content, indicating an enhanced number of Cu−S interactions.[46]

The EXAFS data was then modeled using the Artemis program[34] to obtain Cu-ligand and Cu−Cu coordination numbers (CNs) and nearest neighbor distances (NNDs). The local Cu environment of CuBTC consist of O atoms from the carboxylates in BTC (O$_{BTC}$), a bridging Cu atom, and a flanking water molecule (O$_w$) that may be replaced by loaded S. From the EXAFS fitting shown in Table S1 and Fig. S3,† the local coordination environment around Cu is affected with the inclusion of S. The unloaded CuBTC results in a modeled Cu−O$_{BTC}$ CN close to the ideal value of 4.0, while the inclusion of S reduces the Cu−O$_{BTC}$ CN to 3.43 ± 0.54, 2.83 ± 0.85, and 2.76 ± 0.66 for S : MOF loadings of 0.5, 1.0 and 1.5, respectively. Moreover, the qualitative shift in Cu−O$_{BTC}$ NND from Fig. 2b is captured in the EXAFS modeling (Table S1†) and suggests that the entire MOF structure is slightly perturbed upon sulfur loading. We hypothesize these changes arise from the swelling of the MOF due to more S in the pores. Interestingly, the Cu−Cu structural unit is less affected by the presence of S as only a minimal distortion in Cu−Cu CN is observed with the inclusion of S. The minor changes in Cu coordination environment imply the MOF structure remains largely intact with S-loading.

EXAFS modeling also provides structural insights into the displacement of labile water molecules by S atoms. As noted in a previous study,[44] complete activation of the as-synthesized CuBTC is not possible and residual water coordinated Cu sites (Cu−O$_w$) are observed even after extensive activation procedures. Relative ratios of Cu−O$_w$ to Cu−S backscattering contributions can thus provide insights on the ability of sulfur to displace water. The modeled Cu−S and Cu−O$_w$ CNs and NNDs

are plotted in Fig. 2c and d respectively and presented in Table S1.† The inclusion of 0.5 S : MOF results in a Cu−S CN of 0.49 ± 0.14, which increases to 0.58 ± 0.11 and 0.62 ± 0.08 with S : MOF loadings of 1.0 and 1.5 respectively. Given that a CN of 1.0 is expected for full occupancy of S at every Cu atom, these results indicate that ∼50% of the Cu atoms are coordinated by a S atom for the 0.5 S : MOF loading, with further increases in S loading leading to smaller enhancements in the Cu−S coordination. The non-linear correlation between S loading and Cu−S CN potentially arises from inefficient S incorporation at the Cu site. As the S loading increases, migration to the Cu sites within the MOF pore becomes more difficult. Additionally, clustering of S atoms through formation of S−S bonds could also contribute to this result. Since only one S atom in each cluster contributes to the Cu−S backscattering in the modeled EXAFS, the formation of larger S clusters would lead to only slight increases in the Cu−S CN. Analysis of the Cu−S NND also supports S−S formation at higher S loading. Following the trend observed in DFT interaction distances, the notable increase in Cu−S NND with increasing S content suggests the formation of large S clusters at higher loadings. The Cu−O$_w$ CN similarly changes such that the sum of the Cu−O$_w$ and Cu−S is ∼1.0, indicating that most of the Cu sites are fully coordinated. Furthermore, a minimal change in Cu−O$_w$ NND is obtained from the EXAFS modeling, indicating isolated water molecule and S binding events. Taken together, Cu K-edge XAS demonstrates that S incorporation into CuBTC perturbs the local structure around the Cu centers as a function of S loading.

Thermogravimetric analysis. Thermogravimetric analysis (TGA) is used to examine the different populations of adsorbed sulfur within CuBTC@S (Fig. 3a). The derivative weight loss (d/

dT) indicates regions of mass loss that is attributed to physisorbed and chemisorbed solvents (*e.g.* residual water and ethanol) at temperatures below 190 °C.[48] The total sulfur composition of the CuBTC@S samples is represented by two separate mass loss events. The mass loss at ~230 °C is similar to the thermal decomposition of elemental sulfur (Fig. S4a†) and is correlated to physisorbed sulfur ("Physi-S"),[20,21] which relies on relatively weak intermolecular forces to adsorb in the MOF structure. A smaller second weight loss event is reproducibly observable in the derivative plot at ~320 °C. We assign this second event as the loss of chemisorbed sulfur ("Chemi-S") from direct interactions with the MOF. The lack of such an event prior to complete MOF degradation in the TGA of unloaded CuBTC (Fig. S4b†) further corroborates this assignment. Based on our DFT calculations, we infer these two populations are related to S occupying the open pores and S interacting with the Cu site and BTC π system. The mass loss above 340 °C is based on the degradation of BTC that leads to MOF decomposition.[48,49]

In addition, the sulfur loading extent in CuBTC has a significant impact on the relative concentrations of physisorbed and chemisorbed S. As seen in Fig. 3b, the Chemi-S amount is ~9% at low S : MOF ratios, but increases to 16% at the highest S loading. This finding is aligned with our EXAFS analysis; as sulfur physisorbs in the MOF, more sulfur begins to occupy sites nearest to the MOF framework and becomes available for chemisorption.

The stability of the chemi- and physisorbed sulfur in the MOFs can be observed by the temperature of the mass loss events. Fig. 3c shows that the degradation temperature for both Chemi-S and the MOF increases with higher S loading. This result is in accordance with our computational results: favorable sulfur adsorption sites at the Cu paddlewheel and the BTC π system should lead to higher thermal stability of the MOF. Thus, the similar increase in degradation temperature for BTC and Chemi-S as a function of S loading is further evidence of enhanced sulfur–MOF association.

Raman Spectroscopy. Previous reports of H$_2$S adsorption in CuBTC have used Raman spectroscopy to characterize Cu–S

binding; however, the structural integrity of the MOF was not maintained and offered minimal understanding of S binding in the framework. In our case, CuBTC remains intact upon sulfur loading as evidenced by Powder X-ray Diffraction (PXRD, Fig. S5†) and Fourier Transform Infrared Spectroscopy (FT-IR, Fig. S6†), suggesting Raman spectroscopy is viable for observing these guest–framework interactions. Using previous studies for peak assignments,[44,48,50–52] we focus our attention on the spectral features of the paddlewheel unit, namely the bands of Cu–Cu and Cu–L where L = O$_w$ or S, in CuBTC@S with 1.5 S : MOF loading. A notable shift in the Cu–Cu band from 168 to 185 cm^{-1} upon sulfur loading is observed and implies significant changes to the paddlewheel structure (Fig. S7†). The blue shift of the Cu–Cu band indicates a change in electron density in the Cu–Cu–L unit. Since Cu–O$_w$ is a stronger bond than Cu–S, the substitution of water with sulfur leads to a shift in electron density from the metal–ligand bond to the metal–metal bond. This phenomenon is also reflected in the red shift of the Cu–L band. A broad Cu–O$_w$ band in the unloaded CuBTC sample is seen at 270–300 cm^{-1}, while there is a peak at 260–292 cm^{-1} tentatively assigned to the Cu–S band. These results offer evidence supporting sulfur interaction with the paddlewheel unit and agree with our EXAFS, TGA, and computational findings.

Our combined theoretical and experimental analysis describes in great detail how sulfur interacts with CuBTC and establishes a foundation for understanding sulfur redox chemistry. We have identified two favorable adsorption sites by DFT calculations and used spectroscopic and thermogravimetric techniques to probe these interactions. XANES and EXAFS clearly show that upon sulfur loading, the Cu coordination environment is perturbed in accordance with sulfur interacting with the Cu paddlewheel and the BTC π system. Moreover, the improved thermal stability of CuBTC@S illustrates the favorability of sulfur chemisorption. Raman spectroscopy directly observes the impact of sulfur binding to the Cu site on the Cu–Cu band.

Impact of particle size on Cu–S interaction. With our improved understanding of sulfur–MOF interactions, we shift
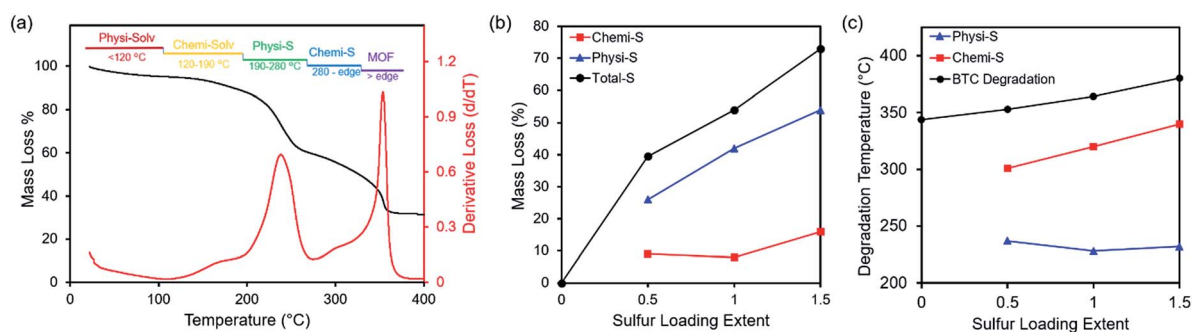

Fig. 3 Thermogravimetric analysis showing (a) a representative CuBTC@S curve (black) and its derivative (red) with the respective thermal decomposition events depicted, and the (b) mass loss and (c) degradation temperature of Chem-S (■) and Physi-S (▲) as function of S loading are also shown. The increase in mass loss of Chemi-S at only high S loading demonstrates a preference for sulfur to physisorb in the MOF. The similar trend in degradation temperatures between CuBTC and Chemi-S suggests that the presence of chemisorbed S interactions stabilizes the overall MOF.

4816 | *J. Mater. Chem. A*, 2018, **6**, 4811–4821

This journal is © The Royal Society of Chemistry 2018

our focus to understand the impact of material properties on Cu–S binding. By manipulating particle size, we speculate that the external surface area and crystal orientation of the MOF particles will play a major role in facilitating electron transfer and polysulfide encapsulation. As shown in Fig. 4, the (111) plane of CuBTC slices through the BTC linker and leads to the lowest density of paddlewheel units on the surface.[53] Conversely, the (001) and (111) planes bisect the Cu paddlewheel, exposing the surface with terminal Cu sites. Changing the morphology and the sizes of the particles will thus alter the ratio of these facets and therefore, affect the number of exposed Cu sites on the surface. We hypothesize that these potential compositional differences will have an impact on sulfur and polysulfide adsorption.

Previous research has reported several procedures to achieve different particle sizes and morphologies, such as modifying the synthesis temperature or employing modulators as capping agents.[36,49] By similarly manipulating the synthesis temperature (−78, −41, 120 °C), we obtain CuBTC with average particle sizes of 0.16, 1.6, and 5.9 μm (Fig. 5 and S8†). In the sample synthesized at −78 °C, all particles exhibit similar morphology and vary in size from 100–250 nm with an average diameter of 0.16 μm. For the synthesis conducted at −41 °C, a distribution polyhedra (<5 μm) is observed with an average particle size of 1.6 μm. In the standard solvothermal syntheses at 120 °C, large polyhedra are observed with particle sizes varying from 3.5–10 μm with an average size of 5.9 μm.

We utilize a variety of techniques to gain insights into the chemical differences arising from particle size and morphology. At the most fundamental level, the bulk structures of all CuBTC samples are identical as observed by PXRD and FT-IR, in agreement with previous literature (Fig. S5 and S6†).[20,44] Although the PXRD patterns have identical peak positions, the relative peak areas of the crystal facets vary with the different syntheses, suggesting differences in preferential orientation. The peak area of the (002) plane, which is analogous to the (001) and contains the highest density of paddlewheels, increases with decreasing particle size relative to the peak area of (222) (Table 1). In contrast, the relative peak areas of (220) to (222) remain similar at all particle sizes. Taken together, the comparatively higher concentration of (002) facets in the small particles implies larger densities of Cu-rich crystallographic
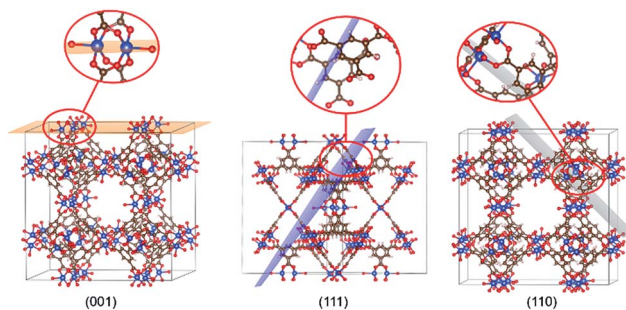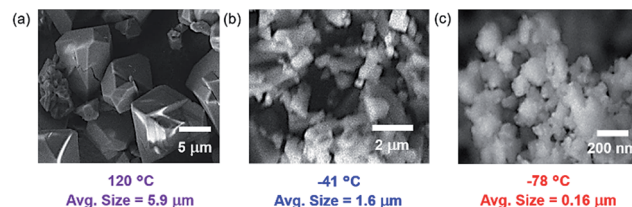

Fig. 5 Electron micrographs showing CuBTC synthesized at (a) 120 °C, (b) −41 °C, and (c) −78 °C.

Table 1 Comparison of (002), (220), and (222) relative peak areas in CuBTC@S, as evidenced by PXRD

CuBTC Sample	Relative peak area (002)/(222)	Relative peak area (220)/(222)
0.16 μm	0.46	0.27
1.6 μm	0.41	0.25
5.9 μm	0.38	0.27

facets and results in a greater number of truncated Cu paddlewheels on the particle surface. Raman spectroscopy is used to analyze compositional differences resulting from particle size and morphology. Comparing 0.16, 1.6, and 5.9 μm CuBTC, all Raman peaks appear at identical energies. However, particle size has an effect on the relative peak intensity of the Cu–Cu paddlewheel signal at 168 cm^{-1} compared to the C=C signal at 1006 cm^{-1} from the BTC linker (Table S2 and Fig. S9†). This observation hints at different ratios of Cu to BTC as a function of particle size.

We also observe similar compositional trends in thermogravimetric analysis. The mass of BTC from the weight loss at ~340 °C is compared to the mass of the copper oxide residue after the complete combustion of the organic components at >400 °C. In the smaller particles (0.16 and 1.6 μm), the Cu : C ratio is significantly higher than that of the large particle size (5.9 μm). This result is also in good agreement with energy dispersive X-ray spectroscopy (EDS, Fig. S10†).

To further confirm these compositional differences, we use atomic absorption spectroscopy (AAS) to examine Cu content in CuBTC as a function of particle size. As seen in Fig. S11,† the Cu absorbance signal, which is normalized to the sample mass of CuBTC, increases linearly with decreasing particle size. The smallest CuBTC particles (0.16 μm) contain the highest concentration of Cu, a result consistent with our Raman spectroscopy and PXRD analysis.

XAS is also employed to compare the local Cu coordination environment in differently-sized particles of CuBTC (Fig. S12 and S13†). The XANES spectra indicate that 0.16 and 1.6 μm CuBTC remain in a 2+ oxidation state, but change drastically with the inclusion of S atoms. With a loading of 1.5 S : MOF, the XANES features of 0.16 and 1.6 μm CuBTC@S are more akin to the 5.9 μm CuBTC@S, whereas different spectral features are noted for the unloaded 0.16 and 1.6 μm CuBTC. This result is consistent with our compositional and PXRD analysis, as a higher quantity of exposed Cu sites interacting with sulfur

Fig. 4 The highlighted planes identify the locations of favorable CuBTC surface termination.[54] (001) and (110) both bisect through a Cu paddlewheel and would result in a Cu-rich surfaces compared to (111).

would lead to increased spectral changes for the smaller particles. EXAFS analysis further demonstrates the differences in local Cu structure in these samples compared to 5.9 μm CuBTC. All CuBTC samples with small particle sizes (with and without S) exhibit significantly reduced Cu–O$_{BTC}$ and Cu–Cu CNs, which suggest the existence of incomplete paddlewheels. Modeled Cu–S CNs of 0.67 ± 0.09 and 0.60 ± 0.04 are obtained for 0.16 and 1.6 μm CuBTC@S samples, similar to values acquired from the 5.9 μm CuBTC@S at the same sulfur loadings. The Cu–S NNDs are also comparable and suggest that Cu–S interactions are similar across all particle sizes. Overall, EXAFS modeling suggests that compared to 5.9 μm CuBTC, the smaller CuBTC particles have more truncated crystal lattices, giving rise to incomplete Cu paddlewheels on the surface of the MOF.

Impact of particle size on polysulfide dissolution. Based on our thermogravimetric and spectroscopic analysis, we reason that the higher availability of S binding sites in 0.16 μm CuBTC particles will lead to improved polysulfide retention in Li–S batteries. We can directly examine this process by employing an open-cell two electrode system and compare the extent of polysulfide dissolution in the first discharge step for 0.16 μm CuBTC@S, 5.9 μm CuBTC@S, and a control S/C cathode at a discharge rate of C/20. At all time points, the control S/C cathode has the highest leaching compared to CuBTC@S cathodes, as evidenced by the color intensity of the electrolyte solution (Fig. 6a). Aliquots of the electrolyte at 0, 4, 8, and 12 h are examined using UV-Vis absorbance spectroscopy (Fig. 6b and S14†). In the absorbance spectra at 4 h, the relative intensity at 420 nm, a peak previously attributed to S$_4^{2-}$ species,[54] is in the order of 0.16 μm CuBTC < 5.9 μm CuBTC < S/C. The differences in the absorbance spectra clearly demonstrate that 0.16 μm CuBTC@S particles retain S$_4^{2-}$ more readily that 5.9 μm CuBTC and S/C. The degree of polysulfide dissolution in these open-cell experiments provide the first indications that particle size indeed plays a role in preventing polysulfide leaching.

Because the equilibria between the polysulfides at various chain length are rapid, the exact speciation of polysulfides is not quantifiable. However, activated CuBTC immersed in prepared electrolyte solutions containing predominantly Li$_2$S$_4$ and Li$_2$S$_6$ species for 2 days shows uptake of the polysulfides, as evidenced

by a color change of the MOF from blue to green. This green color persists even after washing with additional electrolyte and is reminiscent of the color change observed during S$_8$ melt infiltration of CuBTC. Characterization of the resulting MOFs shows the framework remains intact by PXRD and FT-IR (Fig. S15†), suggesting CuBTC is stable to the polysulfides generated under cycling conditions.

Electrochemical cycling of CuBTC@S. There are several critical factors that impact polysulfide reduction and oxidation at the cathode. First, small particles have high external surface areas that enable greater electronic contact with the conductive carbon matrix, resulting in high sulfur utilization and maximal charge capacity. However, the high external surface area also increases contact with the solubilizing electrolyte resulting in higher polysulfide dissolution and poor capacity retention during cycling. In contrast, large particles would suffer from incomplete sulfur utilization, but would benefit from improved capacity retention due to less external contact with the electrolyte. Li *et al.* speculate that the confluence of these factors leads to an optimal "golden size" for ZIF-8 MOF particles, balancing sulfur utilization and minimal polysulfide dissolution.[23] However, this Zn-based MOF does not contain S binding sites and relies solely on the pores for encapsulation. Since CuBTC has sulfur adsorption sites, we expect that manipulating particle size and external surface area may have different effects on polysulfide retention.

We begin our electrochemical analysis of CuBTC@S using cyclic voltammetry (CV) to examine the reduction and oxidation of polysulfides. The potentials of these events match previously reported results for Li–S systems with reduction occurring at ~2.3 V and ~2.0 V and oxidation occurring at ~2.4 V after the first cycle (Fig. S16†).[32,48] Similarly, galvanostatic discharge curves (Fig. 7a) show typical plateaus at 2.3–2.4 V and 2.0–2.1 V, corresponding to long-chain and short-chain sulfur reduction, respectively. The plateau potentials are analogous to the reduction potentials observed in CV, particularly at later cycles (Fig. S17†).

Turning to battery performance, the relationship between maximum capacity and particle size is shown in Fig. 7b. As expected, the 0.16 μm CuBTC@S results in the highest maximum capacity of 679 mA h g^{-1}. A dramatic decrease in
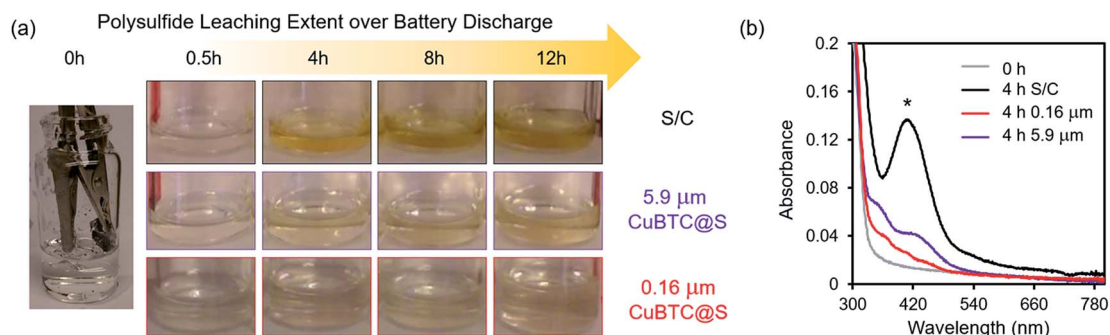

Fig. 6 (a) Electrolyte aliquots taken from 0.16 μm CuBTC, 5.9 μm CuBTC, and S/C electrodes during a galvanostatic discharge of C/20 and (b) UV-Vis absorbance spectra for the aliquots taken at 4 h. As discernable from the photograph and the absorbance spectra, 0.16 μm CuBTC shows the least amount of leached polysulfide, while S/C shows the highest. The peak at 420 nm (*) has been identified to the presence of S$_4^{2-}$.[54]

4818 | *J. Mater. Chem. A*, 2018, **6**, 4811–4821

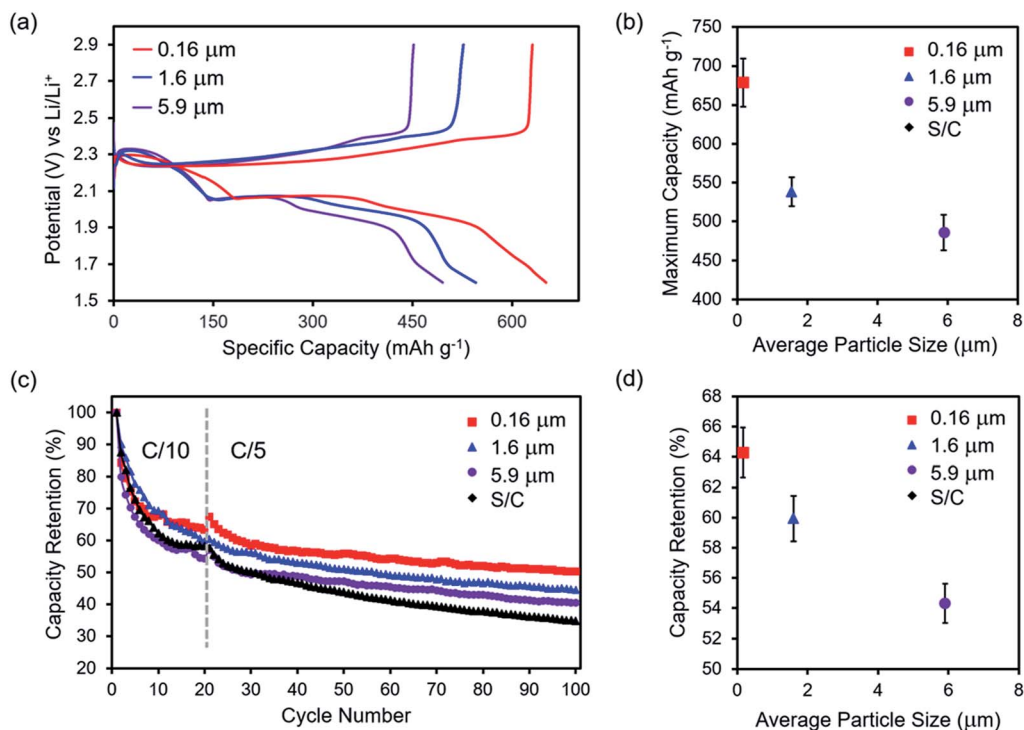This journal is © The Royal Society of Chemistry 2018

Fig. 7 (a) Representative galvanostatic charge and discharge curves for CuBTC@S coin cells after the first discharge cycle at a rate of C/10. (b) The average maximum capacity of 3 cells as a function of particle size. (c) Capacity retention curves for CuBTC@S coin cells shown in (a) over 20 cycles at C/10, followed by 80 cycles at C/5. (d) The average capacity retention of 3 cells of each material after 20 cycles as a function of particle size. In both metrics, 0.16 μm CuBTC@S shows the best performance compared to the other CuBTC@S coin cells.

maximum capacity is seen for the 1.6 and 5.9 μm CuBTC@S. This trend suggests that the large external surface area of small particles affords enhanced sulfur utilization due to high electrical contact and a short electron diffusion pathway for reduction of sulfur species in the MOF.

The cyclability of the battery can be measured by the percentage of capacity retained over a number of cycles. In the capacity retention curves of all the electrodes tested (Fig. 7c), a sharp drop in capacity is observed in the first 20 cycles followed by a gradual decay. The 0.16 μm CuBTC@S shows the best capacity retention of ∼65% in contrast to 1.6 μm (60%) and 5.9 μm (54%) after 20 cycles. This correlation with particle size after 20 cycles is more clearly seen in Fig. 7d. The marked improvement in capacity retention in initial cycles is in agreement with the open-cell discharge experiment described above (Fig. 6). By minimizing initial polysulfide dissolution, higher initial capacities are retained and cyclability is improved. In continued cycling, particle size has less of an effect on the rate of decay for all CuBTC@S samples. Thus, the ability of the MOF to stabilize capacity in the first 20 cycles plays a major role in long-term cycle life. The 0.16 μm particles continue to outperform in capacity retention even after 100 cycles (Fig. S18†). Importantly, all CuBTC@S particles show higher capacity retention than S/C after 100 cycles, demonstrating their superior ability to encapsulate polysulfides.

Capacity retention is dependent on both polysulfide leaching and uptake to maintain high sulfur utilization in the cathode.

Once leached, the dissolved polysulfides can be recovered by the MOF during the charge cycles, a process that has been highlighted previously.[49] We hypothesize that the high external surface area coupled with the increase of surface Cu sites in 0.16 μm CuBTC@S affects the extent of both polysulfide leaching and uptake. To examine differences in polysulfide uptake, we construct CuBTC + S cathodes using a mixture of unloaded CuBTC, elemental sulfur, and carbon binder. The lack of color change upon mechanical mixing suggests that there is a negligible amount of sulfur inside the MOF in CuBTC + S as compared to CuBTC@S. However, the reduction of the sulfur during galvanostatic discharge would generate soluble polysulfides species that can infiltrate into the MOF pores. As noted above, we have observed this process *ex situ* when activated CuBTC is soaked in solutions of synthesized polysulfides (Fig. S15†). This anticipated phenomenon will therefore provide insights into polysulfide recovery.

In CuBTC + S battery cycling experiments, steep drops in capacity are seen in the first discharge cycle at C/10 for all particle sizes (Fig. 8a). The lack of internally adsorbed S in the MOF suggests that the initial capacity of CuBTC + S is mostly attributed to sulfur reduction on the carbon binder. However, the capacity of CuBTC + S particles stabilizes at ∼80% as dissolved polysulfides migrate into the MOF pores. Comparatively, the 0.16 μm CuBTC + S cathode achieves a stable capacity retention more rapidly, which suggests the small particles undergo less irreversible leaching over 20 cycles. This trend is
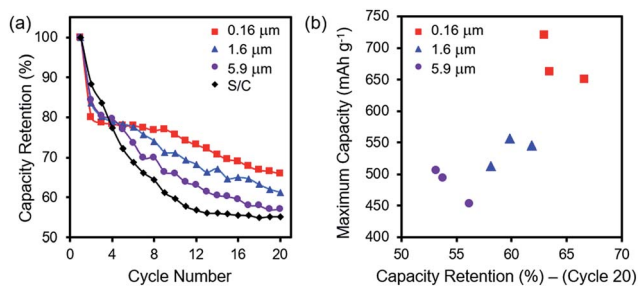
Fig. 8 (a) Capacity retention curves for CuBTC + S cathodes at C/10. Different curve profiles depict differences in polysulfide recovery, with 0.16 μm CuBTC + S showing the best ability to recover polysulfides after the initial capacity decay. (b) Comparison of maximum capacity as a function of capacity retention after 20 cycles for CuBTC@S. Coin cells having the highest performance in both metrics will appear at the top right corner.

even more obvious when compared to the 5.9 μm CuBTC + S, which resembles the exponential capacity decay of S/C. The high external surface area and large concentration of Cu-terminated surfaces in small MOF particles may improve the ability to draw polysulfides into the pore and ameliorate irreversible capacity loss. This enhanced capability to recover polysulfides is also responsible for the greater capacity retention in the first 20 cycles for 0.16 μm CuBTC@S (Fig. 7c).

We compare both metrics, maximum capacity and capacity retention, in the same plot to give an overall summary of battery performance (Fig. 8b). Of the 9 cells tested, 0.16 μm CuBTC@S cathodes clearly outperform in both battery performance metrics. Adding to the findings of previous MOF particle size studies for Li–S batteries,[25] we show that the availability of surface Cu for sulfur binding sites plays a significant role in the overall mechanism of polysulfide dissolution and uptake.

Conclusions

In this study, we provide a detailed analysis on chemical factors that have direct influence on sulfur adsorption in MOFs. Our approach allows us to rationalize device behavior and performance from a molecular standpoint. We have identified and characterized favorable sulfur adsorption sites in CuBTC by DFT, TGA, XAS, and Raman spectroscopy. Moreover, we devised a synthetic approach to probe the impact of key surface attributes, such as particle size and morphology, on battery performance. Using PXRD, TGA, EDS, and AAS, we found that the smaller CuBTC particles contain higher densities of Cu sites, while XAS offers supporting evidence that there are more truncated Cu paddlewheels on the surface of the small MOF particles. Using UV-Vis absorbance spectroscopy, we demonstrated that CuBTC is superior in polysulfide retention to S/C and can bind to S_4^{2-} species. The improved battery performance of CuBTC as a function of particle size suggests that terminal Cu sites may play an important role in promoting polysulfide uptake during cycling. This enhanced ability to adsorb dissolved polysulfides is promising for the development of nanoparticulate CuBTC interlayers for Li–S separator materials. More broadly, we postulate that the incorporation of metal

nanomaterials with judiciously engineered surface defects may significantly mitigate the polysulfide shuttle in traditional S/C cathode materials, such as the use of square planar Cu centers in CuO or CuF_2 nanoparticles. This investigation marks a step towards rational design of material for sulfur adsorption that has important implications for not only Li–S batteries and other energy storage devices, but also in sulfur capture applications for environmental remediation.

Conflicts of interest

There are no conflicts to declare.

Acknowledgements

References

1 G. Zhang, Z.-W. Zhang, H.-J. Peng, J.-Q. Huang and Q. Zhang, *Small Methods*, 2017, 1700134.

2 Y. V. Mikhaylik and J. R. Akridge, *J. Electrochem. Soc.*, 2004, **151**, A1969.

3 C. Liang, N. J. Dudney and J. Y. Howe, *Chem. Mater.*, 2009, **21**, 4724–4730.

4 Q. Pang, D. Kundu and L. F. Nazar, *Mater. Horiz.*, 2016, **3**, 130–136.

5 R. Chen, T. Zhao, T. Tian, S. Cao, P. R. Coxon, K. Xi, D. Fairen-Jimenez, R. Vasant Kumar and A. K. Cheetham, *APL Mater.*, 2014, **2**, 124109.

6 C. Fu, B. M. Wong, K. N. Bozhilov and J. Guo, *Chem. Sci.*, 2016, **7**, 1224–1232.

7 Y. Jin, C. Zhao, Y. Lin, D. Wang, L. Chen and C. Shen, *J. Mater. Sci. Technol.*, 2017, **33**, 768–774.

4820 | *J. Mater. Chem. A*, 2018, **6**, 4811–4821

This journal is © The Royal Society of Chemistry 2018

8 X. Liang, A. Garsuch and L. F. Nazar, *Angew. Chem., Int. Ed.*, 2015, **54**, 3907–3911.

9 Q. Pang, J. Tang, H. Huang, X. Liang, C. Hart, K. C. Tam and L. F. Nazar, *Adv. Mater.*, 2015, **27**, 6021–6028.

10 Z. Li and L. Yin, *ACS Appl. Mater. Interfaces*, 2015, **7**, 4029–4038.

11 M. Zhang, C. Yu, C. Zhao, X. Song, X. Han, S. Liu, C. Hao and J. Qiu, *Energy Storage Materials*, 2016, **5**, 223–229.

12 Z. Li, J. Zhang and X. W. D. Lou, *Angew. Chem., Int. Ed.*, 2015, **54**, 12886–12890.

13 Z. Cui, C. Zu, W. Zhou, A. Manthiram and J. B. Goodenough, *Adv. Mater.*, 2016, **28**, 6926–6931.

14 L. Jia, T. Wu, J. Lu, L. Ma, W. Zhu and X. Qiu, *ACS Appl. Mater. Interfaces*, 2016, **8**, 30248–30255.

15 K. Sun, D. Su, Q. Zhang, D. C. Bock, A. C. Marschilok, K. J. Takeuchi, E. S. Takeuchi and H. Gan, *J. Electrochem. Soc.*, 2015, **162**, A2834–A2839.

16 Y.-S. Su and A. Manthiram, *Nat. Commun.*, 2012, **3**, 1166.

17 M. Safari, C. Y. Kwok and L. F. Nazar, *ACS Cent. Sci.*, 2016, **2**, 560–568.

18 J. Zheng, J. Tian, D. Wu, M. Gu, W. Xu, C. Wang, F. Gao, M. H. Engelhard, J.-G. G. Zhang, J. Liu and J. Xiao, *Nano Lett.*, 2014, **14**, 2345–2352.

19 R. Demir-Cakan, M. Morcrette, F. Nouar, C. Davoisne, T. Devic, D. Gonbeau, R. Dominko, C. Serre, G. Férey and J. M. Tarascon, *J. Am. Chem. Soc.*, 2011, **133**, 16154–16160.

20 Z. Wang, X. Li, Y. Cui, Y. Yang, H. Pan, Z. Wang, C. Wu, B. Chen and G. Qian, *Cryst. Growth Des.*, 2013, **13**, 5116–5120.

21 J. Zhou, R. Li, X. Fan, Y. Chen, R. Han, W. Li, J. Zheng, B. Wang and X. Li, *Energy Environ. Sci.*, 2014, **7**, 2715.

22 J. H. Park, K. M. Choi, D. K. Lee, B. C. Moon, S. R. Shin, M.-K. Song and J. K. Kang, *Sci. Rep.*, 2016, **6**, 25555.

23 L. Bai, D. Chao, P. Xing, L. Tou, Z. Chen, A. Jana, Z. Shen and Y. Zhao, *ACS Appl. Mater. Interfaces*, 2016, **8**, 14328–14333.

24 S. Bai, X. Liu, K. Zhu, S. Wu and H. Zhou, *Nat. Energy*, 2016, **1**, 16094.

25 J. Zhou, X. Yu, X. Fan, X. Wang, H. Li, Y. Zhang, W. Li, J. Zheng, B. Wang and X. Li, *J. Mater. Chem. A*, 2015, **3**, 8272–8275.

26 S. S.-Y. Chui, S. M.-F. Lo, J. P. H. Charmant, A. G. Orpen and I. D. Williams, *Science*, 1999, **283**, 1148–1150.

27 M. A. Gotthardt, R. Schoch, S. Wolf, M. Bauer and W. Kleist, *Dalton Trans.*, 2015, **44**, 2052–2056.

28 C. H. Hendon and A. Walsh, *Chem. Sci.*, 2015, **6**, 3674–3683.

29 H. K. Kim, W. S. Yun, M.-B. Kim, J. Y. Kim, Y.-S. Bae, J. Lee and N. C. Jeong, *J. Am. Chem. Soc.*, 2015, **137**, 10009–10015.

30 K. Vellingiri, A. Deep and K. Kim, *ACS Appl. Mater. Interfaces*, 2016, **8**, 29835–29857.

31 G. Chen, S. Tan, W. J. Koros and C. W. Jones, *Energy Fuels*, 2015, **29**, 3312–3321.

32 C. Petit and T. J. Bandosz, *Dalton Trans.*, 2012, **41**, 4027–4035.

33 C. Petit, B. Mendoza, D. O. Donnell and T. J. Bandosz, *Langmuir*, 2011, **27**, 10234–10242.

34 B. Ravel and M. Newville, *J. Synchrotron Radiat.*, 2005, **12**, 537–541.

35 A. Yakovenko, J. H. Reibenspies, N. Bhuvanesh and H. C. Zhou, *J. Appl. Crystallogr.*, 2013, **46**, 346–353.

36 L. H. Wee, M. R. Lohe, N. Janssens, S. Kaskel and J. A. Martens, *J. Mater. Chem.*, 2012, **22**, 13742.

37 G. Kresse and D. Joubert, *Phys. Rev. B: Condens. Matter Mater. Phys.*, 1999, **59**, 1758–1775.

38 G. Kresse and J. Furthmüller, *Phys. Rev. B: Condens. Matter Mater. Phys.*, 1996, **54**, 11169–11186.

39 Y. Jin, G. Maroulis, X. Kuang, L. Ding, C. Lu, J. Wang, J. Lv, C. Zhang and M. Ju, *Phys. Chem. Chem. Phys.*, 2015, **17**, 13590–13597.

40 J.-J. Chen, R.-M. Yuan, J.-M. Feng, Q. Zhang, J.-X. Huang, G. Fu, M.-S. Zheng, B. Ren and Q.-F. Dong, *Chem. Mater.*, 2015, **27**, 2048–2055.

41 Z. Wang, B. Wang, Y. Yang, Y. Cui, Z. Wang, B. Chen and G. Qian, *ACS Appl. Mater. Interfaces*, 2015, **7**, 20999–21004.

42 Z. Z. Wang, X. Li, Y. Cui, Y. Yang, H. Pan, Z. Z. Wang, C. Wu, B. Chen and G. Qian, *Cryst. Growth Des.*, 2013, **13**, 5116–5120.

43 X. Ji, K. T. Lee and L. F. Nazar, *Nat. Mater.*, 2009, **8**, 500–506.

44 C. Prestipino, L. Regli, J. G. Vitillo, F. Bonino, A. Damin, C. Lamberti, A. Zecchina, P. L. Solari, K. O. Kongshaug and S. Bordiga, *Chem. Mater.*, 2006, **18**, 1337–1346.

45 A. M. Plonka, Q. Wang, W. O. Gordon, A. Balboa, D. Troya, W. Guo, C. H. Sharp, S. D. Senanayake, J. R. Morris, C. L. Hill and A. I. Frenkel, *J. Am. Chem. Soc.*, 2017, **139**, 599–602.

46 M. Du, L. Li, M. Li and R. Si, *RSC Adv.*, 2016, **6**, 62705–62716.

47 E. Borfecchia, S. Maurelli, D. Gianolio, E. Groppo, M. Chiesa, F. Bonino and C. Lamberti, *J. Phys. Chem. C*, 2012, **116**, 19839–19850.

48 M. P. Singh, N. R. Dhumal, H. J. Kim, J. Kiefer and J. A. Anderson, *J. Phys. Chem. C*, 2016, **120**, 17323–17333.

49 F. Wang, H. Guo, Y. Chai, Y. Li and C. Liu, *Microporous Mesoporous Mater.*, 2013, **173**, 181–188.

50 N. R. Dhumal, M. P. Singh, J. A. Anderson, K. Johannes and H. J. Kim, *J. Phys. Chem. C*, 2016, **120**, 3295–3304.

51 K. Tan, N. Nijem, Y. Gao, S. Zuluaga, J. Li, T. Thonhauser and Y. J. Chabal, *CrystEngComm*, 2015, **17**, 247–260.

52 K. Tan, N. Nijem, P. Canepa, Q. Gong, J. Li, T. Thonhauser and Y. J. Chabal, *Chem. Mater.*, 2012, **24**, 3153–3167.

53 S. Amirjalayer, M. Tafipolsky and R. Schmid, *J. Phys. Chem. Lett.*, 2014, **5**, 3206–3210.

54 Q. Zou and Y. C. Lu, *J. Phys. Chem. Lett.*, 2016, **7**, 1518–1525.

This journal is © The Royal Society of Chemistry 2018

J. Mater. Chem. A, 2018, **6**, 4811–4821 | **4821**